

Microrheological model for Kelvin-Voigt materials with micro-heterogeneities

T. N. Azevedo,¹ K. M. Oliveira,¹ H. P. Maia,¹ A. V. N. C. Teixeira,¹ and L. G. Rizzi¹

Departamento de Física, Universidade Federal de Viçosa (UFV), 36.570-900, Viçosa, MG, Brazil.

We introduce a generalization of the Kelvin-Voigt model in order to include and characterize heterogeneities in viscoelastic semisolid materials. By considering a microrheological approach, we present analytical expressions for the mean square displacement and for the time-dependent diffusion coefficient of probe particles immersed in a viscoelastic material described by this model. Besides validating our theoretical approach through Brownian dynamics simulations, we show how the model can be used to describe experimental data obtained for polyacrylamide and laponite gels.

1. INTRODUCTION

Although many viscoelastic materials are observed to have heterogeneous structures¹, *e.g.*, agarose², actin³, collagen⁴, hectorite dispersions⁵, fibril networks⁶ and peptide gels^{7,8}, their theoretical characterization has been the subject of a rather limited number of studies⁹⁻¹¹. Extensive experimental research has shown that heterogeneities, in addition to influencing the formation kinetics of complex materials^{12,13}, can play an important role in their rheological and optical properties¹⁴.

Among the various mechanical models of viscoelasticity, the Kelvin-Voigt (KV) model is one of the simplest theoretical models that can be used to describe viscoelastic materials which display a semisolid response^{15,16}. Basically, it can be characterized by a complex modulus $G^*(\omega)$ given by

$$G^*(\omega) = G_0 + i\eta_0\omega, \quad (1)$$

where G_0 is the storage modulus and η_0 is the viscosity of the material. Although idealized, the KV model has been used to describe the viscoelasticity of several semisolids, and examples include fibrin networks¹⁷, gelatin hydrogels¹⁸, polyurea¹⁹, and laponite gels²⁰. As it happens, a detailed look at the results generally indicates that Eq. 1 works just as a rough approximation and it might be that the departures from such an ideal behaviour could involve, for instance, the presence of heterogeneities in the sample⁵.

Here we consider a microrheology-based approach to propose a generalization of the KV model in order to incorporate the micro-heterogeneities present in semisolid viscoelastic materials. In particular, by assuming that the micro-heterogeneities can be described by position-dependent spring constants $\varepsilon = \varepsilon(\vec{R})$ and drag coefficients $\nu = \nu(\vec{R})$, we are able to describe analytically the power-law behaviour of the time-dependent diffusion coefficient $D(\tau)$ at long times, and relate its exponent to the distribution of spring constants and drag coefficients. Accordingly, we perform stochastic simulations using Brownian dynamics to validate the expressions obtained for $D(\tau)$ and for the mean-squared displacement. Then, we show how our model can be used to describe experimental data obtained from dynamic light scattering (DLS) microrheology for two different kinds of gels.

The manuscript is organized as follows. First, in Sec. 2, we review some aspects of the microrheology of viscoelastic materials that exhibit a Kelvin-Voigt type behaviour (Eq. 1). In Sec. 3, we present the theoretical description of the model introduced here, the Kelvin-Voigt with micro-heterogeneities (KVMH) model, which generalizes the usual KV model. Section 4 presents the validation of our theoretical results through numerical simulations using Brownian dynamics. In Sec. 5 we apply our model in the analysis of data obtained from microrheology experiments, and we show a comparison between the two models to emphasize how the KVMH might be more suitable to describe experimental results when micro-heterogeneities are present in the sample.

2. MICRORHEOLOGY OF SEMISOLID KELVIN-VOIGT (KV) MATERIALS

Before taking into account the micro-heterogeneities, we briefly review how one can consider an analytical approach to describe the microrheological response of the usual Kelvin-Voigt material. In particular, by considering the linear viscoelastic (LVE) regime²¹, one has that the mechanical response of a viscoelastic medium can be probed by the stochastic movement of spherical particles moving through the sample, which are characterized by their mean-squared displacement (MSD) $\langle \Delta r^2(\tau) \rangle \equiv \langle [\vec{r}(\tau) - \vec{r}(0)]^2 \rangle$. Experimentally, the MSD of probes can be obtained through, *e.g.*, particle tracking videomicroscopy or dynamic light scattering techniques²², so that, by considering the following generalized Stokes-Einstein relationship (GSER), one can obtain the compliance of the material as^{23,24}

$$J(\tau) = \frac{3\pi a}{d_e k_B T} \langle \Delta r^2(\tau) \rangle, \quad (2)$$

where k_B and T are the Boltzmann's constant and the absolute temperature of the medium, respectively; a is the radius of the probe particles, and d_e is the Euclidean dimension of the random walk. Importantly, in this work we will only consider disordered and isotropic materials so that the compliance $J(\tau)$ is a scalar function of time. In addition, it is worth noting that the above GSER is derived under the assumption that the radii

of the probe particles are larger than the largest microstructures of the material, and also that the inertia of the probe particles can be neglected²². Under these conditions, the results obtained by the microrheology technique should reproduce the results obtained from bulk rheology. Hence, through the Fourier-Laplace transform of $J(\tau)$, *i.e.*, $\hat{J}(\omega) = \mathcal{L}[J(\tau); s]_{s=i\omega}$, one can obtain the complex modulus $G^*(\omega) = G'(\omega) + iG''(\omega)$ of the material through the following identity^{21,22}

$$G^*(\omega) = \frac{1}{i\omega \hat{J}(\omega)} . \quad (3)$$

Numerically, one can compute the Fourier-Laplace transform, $\hat{J}(\omega)$, by using the method proposed in Ref.²⁵.

Next, for simplicity, we consider a one-dimensional ($d_e = 1$) stochastic movement of a Brownian particle trapped in a harmonic potential, $U(x) = \kappa x^2/2$, so that it can be described by the following overdamped Langevin equation,

$$\zeta \frac{d}{dt} x(t) = -\frac{d}{dx} U(x) + f_a(t) , \quad (4)$$

where ζ is the drag coefficient, $f_a(t)$ is a random force that the surrounding medium exerts on the particle; here the constant κ denotes the strength of a “spring constant” which mimics the properties of the viscoelastic material and characterizes its solid-like response. As it is shown in Ref.²⁶, the solution of the above overdamped Langevin equation yields a mean-squared displacement which corresponds to that of a probe particle immersed in a Kelvin-Voigt material, that is,

$$\langle \Delta x^2(\tau) \rangle = \frac{C}{2\gamma} [1 - \exp(-2\gamma\tau)] , \quad (5)$$

where $\gamma = \kappa/\zeta$. As discussed in Ref.²⁷, the fluctuation-dissipation theorem links the constant C to the auto-correlation function of the “forces”, $\tilde{f}_a = f_a/\zeta$, which is given by $\langle \tilde{f}_a(\tau) \tilde{f}_a(\tau') \rangle = C\delta(\tau - \tau')$. By considering that $\langle \Delta x^2(\tau) \rangle = \langle x^2(\tau) \rangle$ with $x(0) = 0$, and assuming that the equipartition theorem holds, one has that $\kappa \langle \Delta x^2(\infty) \rangle = \kappa \langle x^2(\infty) \rangle = k_B T$, which leads to $C = 2k_B T/\zeta$. That value is consistent with a force auto-correlation function that is given by $\langle f_a(\tau) f_a(\tau') \rangle = 2k_B T \zeta \delta(\tau - \tau')$.

Hence, from Eq. 5, one finds that the MSD of the usual KV is given by

$$\langle \Delta x^2(\tau) \rangle = \frac{k_B T}{\kappa} \left[1 - \exp\left(-2\frac{\tau}{\tau_c}\right) \right] , \quad (6)$$

where $\tau_c = (\gamma)^{-1}$ is a characteristic (*i.e.*, corner) time. Accordingly, Eq. 6 displays a linear (*i.e.*, normal diffusive) behaviour $\langle \Delta x^2(\tau) \rangle \approx 2(k_B T/\zeta)\tau$ for $\tau \ll \tau_c$, and a constant value, $\langle \Delta x^2(\tau) \rangle \approx k_B T/\kappa$, when $\tau \gg \tau_c$, indicating that the displacements of the probe particle are restricted to a region of the sample at long times. In addition, one can evaluate the time-dependent diffusion coefficient as

$$D(\tau) = \frac{1}{2d_e} \frac{d}{d\tau} \langle \Delta r^2(\tau) \rangle = \frac{k_B T}{\kappa \tau_c} \exp\left(-2\frac{\tau}{\tau_c}\right) , \quad (7)$$

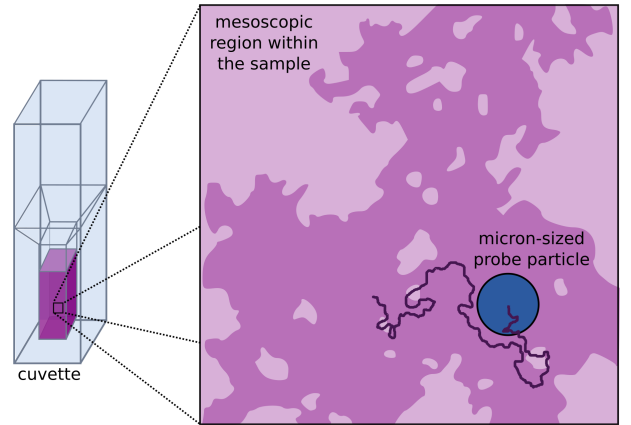


FIG. 1. Illustration of the heterogeneous microrheology that is described by the KVMH model, where a single micron-sized probe particle immersed in a semisolid experiences a viscoelastic response that is characterized by a spring constant $\varepsilon(\vec{R})$ and a drag coefficient $\nu(\vec{R})$, which are locally-defined near a mesoscopic region denoted by \vec{R} .

where the right side of the above identity does not depend on d_e since $\langle \Delta r^2(\tau) \rangle = d_e \langle \Delta x^2(\tau) \rangle$ for isotropic materials. Now, by considering the GSER given by Eq. 2, one can use Eq. 6 to obtain the compliance $J(\tau)$, which can be readily identified as the compliance of a KV material¹⁵. As shown in Ref.²⁶, one can use the corresponding compliance $J(\tau)$ to evaluate both the storage, $G'(\omega)$, and the loss modulus, $G''(\omega)$, of the material through Eq. 3, that is,

$$G^*(\omega) = G'(\omega) + iG''(\omega) = \frac{\kappa}{3\pi a} + i\frac{\zeta}{6\pi a}\omega . \quad (8)$$

By comparing this last expression with Eq. 1, one can identify $G_0 = \kappa/3\pi a$ and $\eta_0 = \zeta/6\pi a$. We note that, since the measured moduli should not exhibit any dependence on the radius a of the probe particle, both $\kappa = \kappa(a)$ and $\zeta = \zeta(a)$ are expected to display a linear dependence on a . Thus, based on the microrheology of a KV material, one should have that the spring constant and the drag coefficient are respectively related to the plateau modulus and the viscosity of the KV material, that is, $\kappa = 3\pi a G_0$ and $\zeta = 6\pi a \eta_0$.

3. KELVIN-VOIGT MODEL WITH MICRO-HETEROGENEITIES (KVMH)

Now, in order to take into account the micro-heterogeneities, we assume that the sample has a region-dependent drag coefficients $\nu = \nu(\vec{R})$, where \vec{R} is the position of a mesoscopic region within the sample, as illustrated in Fig. 1. Although the elastic properties in different regions of the system are heterogeneous throughout the sample, we assume that, locally, the drag coefficient is constant within a given mesoscopic region so that

the probe particle will not experience drastic changes in the viscoelastic properties of the medium while being in that region. Also, because the probe particle is trapped by a harmonic potential, which is defined by the local spring constant $\varepsilon = \varepsilon(\vec{R})$, it is not expected to leave that mesoscopic region during the typical time scale of the experiments $\tau_e \gg \tau_c$.

In the following, we discuss both the theoretical and computational aspects involved in the description of the KVMH.

3.1. MSD and the distribution of micro-heterogeneities

Following the approach introduced in Ref.¹¹, we assume that the MSD (i.e., averaged over trajectories of probe particles which experience different viscoelastic properties due to the micro-heterogeneities) can be evaluated as

$$\langle \Delta x^2(t) \rangle = \int \langle \Delta x^2(t) \rangle_\xi \rho(\xi) d\xi, \quad (9)$$

where the locally defined microrheological properties of mesoscopic regions within the system are incorporated into the model through the distribution $\rho(\xi)$. As in Ref.¹¹, here we define $\rho(\xi)$ as a gamma distribution²⁸, that is,

$$\rho(\xi) = \frac{\xi^{-(1+p)} e^{-\xi}}{\Gamma(p)}, \quad (10)$$

with $\Gamma(p)$ being the usual gamma function and p is an exponent that characterizes the distribution of the region-dependent variable $\xi = \xi(\vec{R})$, so that the mean value of ξ is given by

$$\bar{\xi} = \int_0^\infty \xi \rho(\xi) d\xi = p. \quad (11)$$

In particular, by considering that $\gamma_\xi = \kappa/\nu_\xi$, with the local drag coefficient given by

$$\nu_\xi \equiv \frac{p}{\xi} \zeta, \quad (12)$$

it follows from the analogy with Eq. 5 that

$$\langle \Delta x^2(\tau) \rangle_\xi = \frac{C_\xi \nu_\xi}{2\kappa} \left[1 - \exp\left(-2\frac{\kappa}{\nu_\xi} \tau\right) \right], \quad (13)$$

where the constant C_ξ can be estimated by assuming that the equipartition theorem is locally valid, that is,

$$C_\xi = 2 \left(\frac{k_B T}{\zeta} \right) \left(\frac{\xi}{p} \right), \quad (14)$$

with ξ distributed according to Eq. 10. Interestingly, for short times, Eq. 13 yields $\langle \Delta x^2(\tau) \rangle_\xi \approx C_\xi \tau$, so that Eq. 9

together with Eq. 11 leads to the usual linear diffusive behaviour, that is,

$$\langle \Delta x^2(\tau) \rangle \approx 2 \left(\frac{k_B T}{\zeta} \right) \tau. \quad (15)$$

On the other hand, at later times, Eq. 13 yields

$$\langle \Delta x^2(\tau) \rangle_\xi \approx \frac{C_\xi \nu_\xi}{2\kappa} = \frac{k_B T}{\kappa}, \quad (16)$$

so that, because the distribution $\rho(\xi)$ is normalized, Eq. 9 also leads to a ξ -independent result for the total MSD, that is,

$$\langle \Delta x^2(\tau) \rangle \approx \int_0^\infty \left(\frac{k_B T}{\kappa} \right) \rho(\xi) d\xi = \frac{k_B T}{\kappa}. \quad (17)$$

Obviously, by considering $\rho(\xi)$ given by Eq. 10, one can evaluate the expression for the MSD more generally from Eq. 13. Indeed, by performing the corresponding integral²⁹ one finds from Eq. 9 that

$$\langle \Delta x^2(\tau) \rangle = \frac{k_B T}{\kappa} \left[1 - \left(\frac{2\tau}{p\tau_c} + 1 \right)^{-p} \right]. \quad (18)$$

In addition, the time-dependent diffusion coefficient $D(\tau)$, which can be evaluated through the derivative of the MSD (see, e.g., Eq. 7), is given by

$$D(\tau) = \frac{k_B T}{\kappa \tau_c} \left(\frac{2\tau}{p\tau_c} + 1 \right)^{-(1+p)}. \quad (19)$$

It is worth emphasizing that, at later times, the above result indicates that the time-dependent diffusion coefficient behaves like a power-law, that is, $D(\tau) \propto \tau^{-(1+p)}$. Essentially, this is the main feature that distinguishes the KVMH model from the usual KV model. Indeed, the distinction between an exponential, Eq. 7, and a power-law, Eq. 19, can be observed in microrheological experiments, so it should be used to indicate the presence of micro-heterogeneities as the exponent p is the quantity that defines the distribution $\rho(\xi)$ (Eq. 10).

One should note that, for large values of p , the negative term in the MSD given by Eq. 18 goes to an exponential function, *i.e.*, $e^{-z} = \lim_{p \rightarrow \infty} (1+z/p)^{-p}$, so that it recovers the MSD obtained for the usual KV model (Eq. 6). Also, large p leads the distribution $\rho(\xi)$ (Eq. 10) to be more localized around a prominent peak, which means that only a particular value ξ^* will contribute to the average of ξ , fading out the effect of the micro-heterogeneities.

In addition, it is worth noting that the MSD given by Eq. 18 can be thought of as a particular case of a general result obtained in Ref.¹¹, which reads

$$\langle \Delta x^2(\tau) \rangle = \frac{k_B T}{\kappa} \left\{ 1 - \left[\left(\frac{\tau}{\tau^*} \right)^{n^*} + 1 \right]^{-\alpha} \right\}, \quad (20)$$

where τ^* is a characteristic time, α is a parameter related to a gamma distribution just like Eq. 10, and n^*

is an exponent related to the nature of the diffusive behaviour that can be eventually observed at short times. As discussed in Ref.¹¹, where a generalized overdamped Langevin approach is used, the cases where $0.5 < n^* < 1$ denote a non-Markovian subdiffusive behaviour, while $n^* = 1$ correspond to the case where the normal diffusive behaviour of the probe particles is Markovian, as for the KV and KVMH models (see Eqs. 15 and 18).

Finally, it is important to note that, as also pointed out in Ref.¹¹, the use of a gamma distribution $\rho(\xi)$ (Eq. 10) has been established because of the link between the effective elastic constants and the size of clusters of particles with a given size^{30–32}. Besides the relationship to the cluster sizes, gamma distributions are not only derived from kinetic equations³² which can be related to the relaxation times distributions $H(\lambda)$ observed experimentally from mechanical spectroscopy³³, but are also observed in the disordered networks generated by numerical simulations^{34,35}.

3.2. Related distributions: elastic constants ε and characteristic times λ

As it will become clear in the Sec. 4, the distribution $\rho(\xi)$ given by Eq. 10 can be interpreted either in terms of local elastic constants ε or, alternatively, in terms of local characteristic times λ , both which will be given by generalized gamma distributions²⁸. In particular, if we consider that $\varepsilon = (\kappa/p)\xi$, the distribution of local spring constants $\rho(\varepsilon)$ will be given by $\rho(\varepsilon) = \rho(\xi)|_{\xi=p\varepsilon/\kappa} (\partial\xi/\partial\varepsilon)$, that is,

$$\rho(\varepsilon) = \left(\frac{p}{\kappa}\right)^p \frac{\varepsilon^{p-1}}{\Gamma(p)} \exp\left(-\frac{p\varepsilon}{\kappa}\right), \quad (21)$$

so that the average value of the effective spring constants will be given by

$$\bar{\varepsilon} = \left(\frac{\kappa}{p}\right) \bar{\xi} = \kappa. \quad (22)$$

Furthermore, by considering that the local characteristic time is given by $\lambda = p\tau_c/\xi$, one can obtain the distribution $H(\lambda)$ from the distribution $\rho(\xi)$ as $H(\lambda) = \rho(\xi)|_{\xi=p\tau_c/\lambda} (\partial\xi/\partial\lambda)$, which yields

$$H(\lambda) = \frac{1}{\Gamma(p)} \frac{1}{p\tau_c} \left(\frac{p\tau_c}{\lambda}\right)^{1+p} \exp\left(-\frac{p\tau_c}{\lambda}\right). \quad (23)$$

Accordingly, in this last case, the average value of the characteristic times λ is given by

$$\bar{\lambda} = \int \lambda H(\lambda) d\lambda = \frac{\tau_c}{p-1}. \quad (24)$$

We note that, although $\bar{\lambda}$ is different from the mean characteristic time τ_c , the average value of the reciprocal of the characteristic times, λ^{-1} , will be given in terms of τ_c as

$$\overline{\lambda^{-1}} = \int \frac{1}{\lambda} H(\lambda) d\lambda = \frac{1}{\tau_c}. \quad (25)$$

3.3. Time-dependent van Hove distributions

To characterize the movement of probe particles, one can also compute the van Hove distributions, which can be easily determined from experiments and gives the probability of a given displacement x after a time interval τ . Analytically, one can evaluate the position distributions $f(x, \tau)$ as

$$f(x, \tau) = \int f_\xi(x, \tau) \rho(\xi) d\xi, \quad (26)$$

where²⁶

$$f_\xi(x, \tau) = \left(\frac{1}{2\pi\langle\Delta x^2(\tau)\rangle_\xi}\right)^{1/2} \exp\left(-\frac{x^2}{2\langle\Delta x^2(\tau)\rangle_\xi}\right), \quad (27)$$

corresponds to the position distribution observed from the random movement of a probe in a particular mesoscopic region of the sample. The normal distribution is typically expected for $f_\xi(x, \tau)$ because we are assuming that, locally, the random moves of a probe particle can be still described by a Gaussian process.

Unfortunately, it is difficult to evaluate the full analytic expression for $f(x, \tau)$, i.e., for any arbitrary time interval τ , from Eq. 26 considering Eq. 27 with the MSD given by Eq. 18. However, if we consider the approximation for the MSD at short times ($\tau \ll \tau_c$), that is, $\langle\Delta x^2(\tau)\rangle_\xi \approx (2k_B T \xi / \zeta p) \tau$, with ξ being a random variable that follows the distribution $\rho(\xi)$ given by Eq. 10, Eq. 26 leads to²⁹

$$f(x, \tau) = \frac{2C_\tau (C_\tau x)^{p-1/2}}{\sqrt{\pi}\Gamma(p)} K_{p-1/2}(2C_\tau |x|), \quad (28)$$

where $C_\tau = (\zeta p / 4k_B T \tau)^{1/2}$ and $K_\phi(x)$ is the modified Bessel function of the second kind of order ϕ . On the other hand, at later times, at the steady state ($\tau \gg \tau_c$), the MSD will be independent of ξ and τ (see Eq. 16), so that the van Hove distribution evaluated through Eqs. 26 and 27 should be given by a normal distribution as well, that is,

$$f(x) = \sqrt{\frac{\kappa}{2\pi k_B T}} \exp\left(-\frac{\kappa x^2}{2k_B T}\right). \quad (29)$$

4. NUMERICAL SIMULATIONS

As discussed in Ref.²⁶, the trajectories of the probe particles can be obtained through overdamped Brownian dynamics simulations by considering an Euler integration scheme which leads to the following discretized equation

$$x_{i+1} = x_i - \frac{\kappa}{\zeta} x_i \Delta\tau + \sqrt{2\frac{k_B T}{\zeta}} \Delta\tau N(0, 1), \quad (30)$$

with $\Delta t = t_{i+1} - t_i$, $x_i = x(t_i)$, $x_0 = 0$, and $N(0, 1)$ being a Gaussian variable with zero mean and variance equal

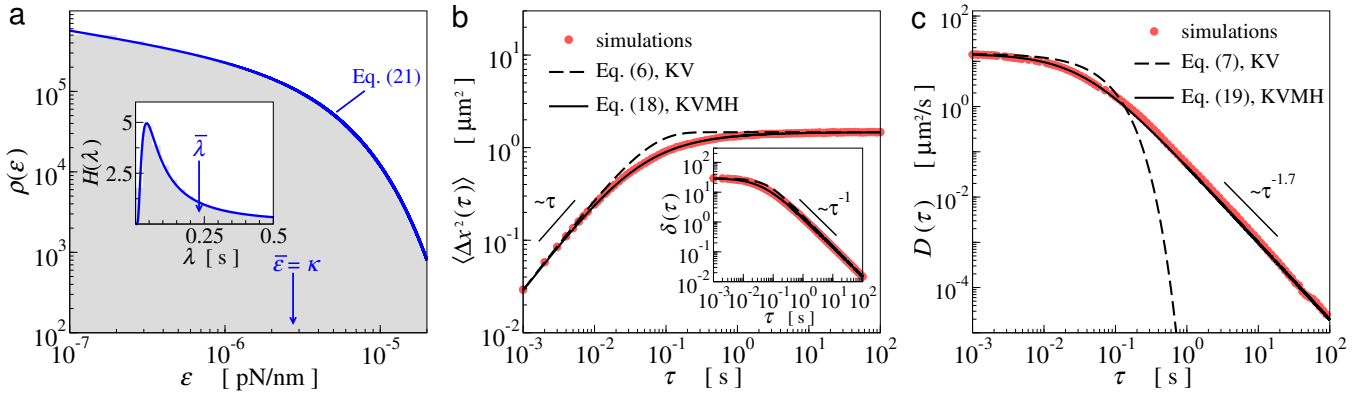


FIG. 2. Numerical and theoretical results obtained for the KV and KVMH models. (a) Histogram (grey) and analytical distribution (continuous blue line, Eq. 21) of local elastic constants $\rho(\varepsilon)$ with $p = 0.7$ and $\kappa = 2.8 \times 10^{-6}$ pN/nm. Inset: Histogram and analytical distribution (Eq. 23) of characteristic times $H(\lambda)$. (b) Mean-squared displacement $\langle \Delta x^2(\tau) \rangle$. Inset: Ratio $\delta(\tau) = \langle \Delta x^2(\tau) \rangle / \tau$. (c) Time-dependent diffusion coefficient $D(\tau)$. Filled (red) circles correspond to results obtained from numerical simulations with $T = 298$ K, $\kappa = 2.8 \times 10^{-6}$ pN/nm, $\zeta = 0.28 \times 10^{-6}$ pN.s/nm, $N_t = 10^5$ trajectories and $\Delta\tau = 10^{-4}$ s, while the (black) lines denote results obtained from the KV model (dashed lines), Eqs. 6 and 7, and the KVMH model (continuous lines), Eqs. 18 and 19 with $p = 0.7$, where in the expressions for both models we assume the same values for T , κ , and ζ as in the simulations.

to one. In order to consider the micro-heterogeneities present in the system, we assume a position-dependent drag coefficient $\nu_n = \nu(\vec{R}_n)$, so that Eq. 30 becomes

$$x_{i+1} = x_i - \frac{\kappa}{\nu_n} x_i \Delta\tau + \sqrt{\frac{2k_B T}{\nu_n}} \Delta\tau N(0, 1) \quad (31)$$

Hence, the n -th particle will display a single trajectory that probes the n -th mesoscopic region within the sample (see, e.g., Fig. 1). Here, just as in the relationship established by Eq. 12, we consider that

$$\nu_n = p \frac{\zeta}{\xi_n}, \quad (32)$$

with ξ_n being the n -th random variable sampled according to a gamma distribution given by Eq. 10. Hence, with this choice of ν_n , the discretized Langevin equation, Eq. 31, becomes

$$x_{i+1} = x_i - \left(\frac{1}{p} \frac{\kappa}{\zeta} \xi_n \right) x_i \Delta\tau + \sqrt{2 \frac{k_B T}{\kappa} \left(\frac{1}{p} \frac{\kappa}{\zeta} \xi_n \right)} \Delta\tau N(0, 1), \quad (33)$$

which can be used to simulate the n -th distinct mesoscopic region within the sample that displays slightly different viscoelastic properties. Interestingly, one can also interpret Eq. 33 as an expression for a medium that displays different local spring constants which are given by

$$\varepsilon_n = \left(\frac{\kappa}{p} \right) \xi_n, \quad (34)$$

just as defined in Section 3.2. Besides, it is worth noting that, based on Eq. 33, one has that the time-correlation

function of the forces acting at the n -th probe particle can be written as²⁷

$$\langle \tilde{f}_a(\tau) \tilde{f}_a(\tau') \rangle_n = 2 \frac{k_B T}{\kappa} \frac{\varepsilon_n}{\zeta} \delta(\tau - \tau'), \quad (35)$$

which means that the fluctuation-dissipation theorem is locally valid, where *local* here means that the probe's trajectory is spatially localized within a mesoscopic region which is characterized by a single value of ε_n .

Figure 2 presents results obtained from numerical simulations that not only validate the algorithm we have just described but also demonstrate the theoretical results obtained from the KVMH model, illustrating its main differences from the usual KV model. In Fig. 2(a) we include the distribution of local spring constants $\rho(\varepsilon)$, Eq. 21, and the corresponding distribution of characteristic times $H(\lambda)$, Eq. 23, that were used to perform the simulations. Figure 2(b) shows the MSDs obtained for the KV and KVMH models, given by Eqs. 6 and 18, respectively. Accordingly, the two models display the same asymptotic behaviours for short and long times, where we observe a linear behaviour, $\langle \Delta x^2(\tau) \rangle \approx 2(k_B T / \zeta)\tau$, and a plateau, $\langle \Delta x^2(\tau) \rangle \approx k_B T / \kappa$, respectively. Also, as the numerical results presented in the inset panel in (b) indicate, the ratio $\delta(\tau) = \langle \Delta x^2(\tau) \rangle / \tau$ follows the expected behaviour according to the analytical results denoted by the black lines. For instance, for the KVMH, $\delta(\tau)$ is given by Eq. 15 divided by τ , so it is constant at short times, and, at later times, it displays an algebraic decay proportional to τ^{-1} , with $\delta(\tau)$ given by a constant, i.e., Eq. 17, divided by τ .

Even though the difference between the KV and KVMH models can be noticed from the results obtained for the MSD at intermediate times, the difference is better observed in the behaviour of the time-dependent diffusion coefficient $D(\tau)$. As shown in Fig. 2(c), the KV

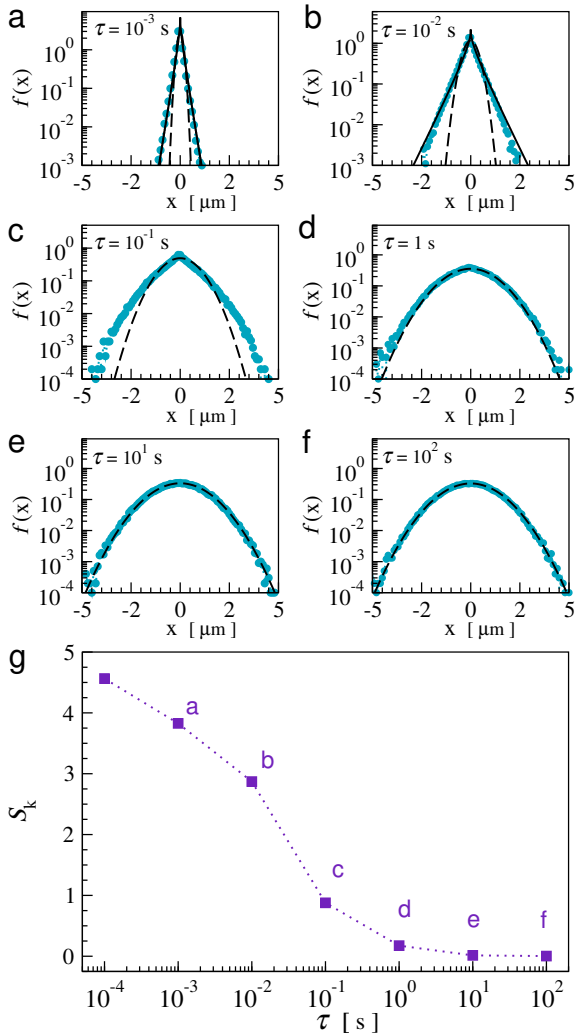


FIG. 3. (a)-(f) Position distributions $f(x, \tau)$ at different times τ determined for the KVMH model. Filled symbols correspond to histograms evaluated from $N_t = 10^5$ trajectories obtained from numerical simulations in one dimension ($d_e = 1$) as described in Sec. 4, with $T = 298$ K, $\kappa = 2.8 \times 10^{-6}$ pN/nm, $\zeta = 0.28 \times 10^{-6}$ pN.s/nm, $p = 0.7$, and $\Delta\tau = 10^{-4}$ s. Continuous black lines denote the expected analytical distribution for short times given by Eq. 28, while dashed black lines correspond to Gaussian distributions, Eq. 29. (g) Excess kurtosis $S_k(\tau)$ given by Eq. 37.

model displays an exponential decay, Eq. 7, while the KVMH model exhibits a power-law behaviour, Eq. 19, with $D(\tau) \propto \tau^{-1.7}$ for $p = 0.7$. We note that, in practice, the derivative used to compute the diffusion coefficient was numerically determined from the MSD through the expression $D(\tau) = \langle \Delta x^2(\tau) \rangle p(\tau) / 2\tau$, where $p(\tau) = \text{dln} \langle \Delta x^2(\tau) \rangle / \text{dln} \tau$ is the effective exponent of the MSD, obtained here through a numerical linear regression. It is worth mentioning that the observed power-law behaviour of $D(\tau)$ at later times is in agreement with the experimentally observed behaviour of certain hydrogels³⁶.

In Fig. 3(a)-(f) we show the van Hove distributions $f(x, \tau)$ obtained numerically from the simulations at different times τ , together with the expected analytical distribution given by Eq. 28 at short times (continuous lines) and the Gaussian distributions predicted by the KV model defined in Sec. 2 given by Eq. 29 (dashed lines). In order to generate the Bessel function $K_\phi(x)$ we used the built-in function `scipy.special.kv` of the Scipy library³⁷. For small orders ϕ and for $x > 0$, the algorithm uses the following integral representation²⁹

$$K_\phi(x) = \sec\left(\frac{\phi\pi}{2}\right) \int_0^\infty \cos(x \sinh(t')) \cosh(\phi t') dt', \quad (36)$$

for $-1 < \text{Re}\{\phi\} < 1$.

Figure 3 indicates that the distributions obtained at short times are similar to Eq. 28 and approach Gaussian distributions at later times. In order to assess the deviation of the obtained distributions from Gaussian distributions, we obtain the excess kurtosis which is defined as⁵

$$S_k(\tau) = \sum_{j=1}^{N_t} \frac{[x_j(\tau) - \bar{x}(\tau)]^4}{(N_t - 1)[\sigma_x(\tau)]^4} - 3, \quad (37)$$

where N_t is the number of trajectories, \bar{x} is the mean and σ_x is the standard deviation of the distribution. Figure 3(g) shows that $S_k(\tau)$ obtained for the distributions at different times is higher for short times, but it approaches zero at later times, as the excess kurtosis is expected to be zero for Gaussian distributions.

A non-zero excess of kurtosis at short times τ is precisely what is observed during sol-gel transition gelation examined through microrheology experiments^{5,20,38}. In those experiments, a zero excess of kurtosis is observed for short gelation times at any time τ (characterizing the sol phase of the samples) followed by an increase in excess kurtosis as the sample jellifies and becomes more heterogeneous (characterizing their gel phase). In these cases, the increase in the excess kurtosis can be clearly associated with the presence of heterogeneous structures in the semisolid materials.

5. APPLICATION OF THE KVMH MODEL TO EXPERIMENTAL DATA

In this section, we present a comparison between the expressions obtained from the KVMH model and some experimental data to further validate our approach.

5.1. Results for polyacrylamide gels from Ref.³⁹

We first include in Fig. 4 the comparison between the KV and KVMH models and the experimental data extracted from Ref.³⁹, where microrheology experiments

were carried out for chemically cross-linked polymer polyacrylamide gels. The experiments were done with the particle tracking technique²¹ using positively charged aldehyde amidine polystyrene spheres with radius $a = 0.05 \mu\text{m}$ at room temperature ($T = 298 \text{ K}$).

As it can be seen in Fig. 4(a), the experimental data obtained for the MSD presents an approximately linear behaviour at short times and a plateau at long times, just as the expressions derived for the KV and the KVMH models, with the latter showing a slightly better agreement with the experimental data. In Fig. 4(b) we include the experimentally determined³⁹ van Hove distribution $f(x, \tau)$ at time $\tau = 0.1 \text{ s}$, together with the distribution obtained from numerical simulations using the parameters obtained from the fit of the MSD determined for the KVMH model displayed in 4(a). Accordingly, the good agreement between the numerical and experimental distributions $f(x, \tau)$ in Fig. 4(b), including their matching non-Gaussianity, serves as an indirect validation of the gamma distribution, Eq. 10, used to define the KVMH.

Figure 4(c) includes results for the time-dependent diffusion coefficient $D(\tau)$. It is worth mentioning that, due to the noisy nature of the MSD data, the diffusion coefficient $D(\tau)$ was obtained from a smoothed interpolation of the experimental data (see Ref.⁴⁰ for a description of the algorithm). The idea is that, given a sequence of N_k measurements $\{v_1, v_2, \dots, v_{N_k}\}$, one minimizes

$$\varphi \sum_{j=1}^{N_k} [v_j(\tau) - h_j(\tau)]^2 + \sum_{j=1}^{N_k-2} [h_{j+2}(\tau) - 2h_{j+1}(\tau) + h_j(\tau)], \quad (38)$$

where $h_j(\tau)$ are the values that interpolates the data and φ is a positive real smoothing parameter. The larger φ the more the solution converges to the measured sequence. The smaller φ the smoother the interpolation. Here the values φ were chosen in a way that $D(\tau)$ does not display any oscillatory behaviour. The comparison to experimental results in Fig. 4(c) evidences the difference between the models' predictions, from where one can see that the exponential decay of $D(\tau)$ predicted by the KV model does not fit satisfactorily the experimental data very well. Conversely, the value of $p = 1.67$ determined from $D(\tau)$ given by the KVMH suggests that the presence of micro-heterogeneities in this gel are relevant, reinforcing the results presented in Fig. 4(b).

Finally, we include in Fig. 4(d) a comparison to show how the models perform in describing the behaviour of the shear moduli $G'(\omega)$ and $G''(\omega)$. As mentioned in Sec. 2, Eqs. 2 and 3 allow us to obtain the complex shear modulus $G^*(\omega)$ of the material from the MSD. As we were not able to derive exact analytic expressions for the complex modulus $G^*(\omega)$ of the KVMH, we numerically

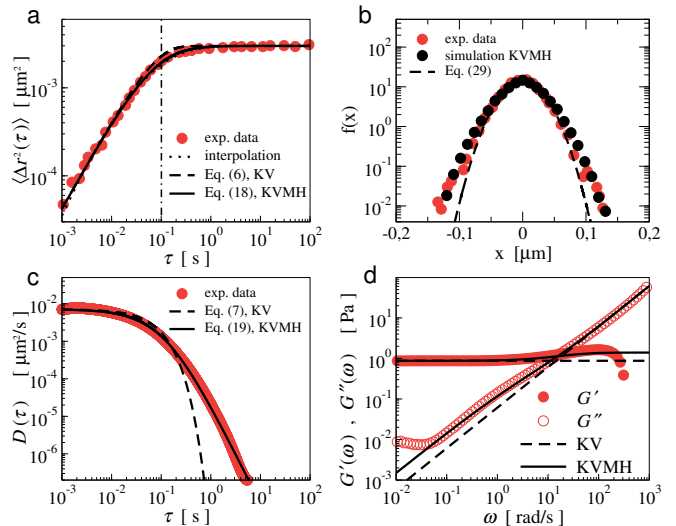


FIG. 4. Comparison between the experimental data for polyacrylamide gels (filled red circles) extracted from Ref.³⁹ and the results obtained from the usual KV model with $T = 298 \text{ K}$, $\kappa = 2.75 \text{ pN}/\mu\text{m}$, $\tau_c = 0.14 \text{ s}$, and the KVMH with the same parameters but a distribution characterized by $p = 1.67$. (a) MSD $\langle \Delta r^2(\tau) \rangle$. The vertical dash-dotted line indicates $\tau = 0.1 \text{ s}$. (b) Position distributions $f(x, \tau)$ at time $\tau = 0.1 \text{ s}$. Filled red and black circles denote the distributions obtained from experiments and numerical simulations, respectively, while the dashed line corresponds to a Gaussian distribution, Eq. 29. (c) Time-dependent diffusion coefficient $D(\tau)$ (here the experimental estimates were obtained from a smoothed interpolation⁴⁰ using Eq. 38 with $\varphi = 0.003$). (d) Storage modulus $G'(\omega)$ (filled circles) and loss modulus $G''(\omega)$ (open circles), obtained from $\langle \Delta r^2(\tau) \rangle$ via Eqs. 2 and 3, with $\hat{J}(\omega)$ obtained through Eq. 39 using the numerical method described in Ref.²⁵.

compute the Laplace-Fourier transform $\hat{J}(\omega)$ through²⁵

$$-\omega^2 \hat{J}(\omega) = i\omega J(0) + (1 - e^{-i\omega\tau_1}) \frac{(J_1 - J(0))}{\tau_1} + \hat{J}_\infty e^{-i\omega\tau_N} + \sum_{k=2}^N \left(\frac{J_k - J_{k-1}}{\tau_k - \tau_{k-1}} \right) (e^{-i\omega\tau_{k-1}} - e^{-i\omega\tau_k}), \quad (39)$$

where one can assume that $J(0) = \lim_{\tau \rightarrow 0} J(\tau) = 0$ and $\hat{J}_\infty = \lim_{\tau \rightarrow \infty} dJ(\tau)/d\tau = 0$. Figure 4(d) indicates that the shear moduli obtained from the KV model deviate from the experimental data, especially at low frequencies for the loss modulus $G''(\omega)$ and at high frequencies for the storage modulus $G'(\omega)$, while the KVMH yields a better correspondence.

5.2. Dynamic light scattering (DLS) experiments

Next, we present results obtained from dynamic light scattering (DLS) experiments performed by our group. Hence, in this Section, we include a brief description of

the methods and experimental setup. The DLS measurements were made using a laser with a wavelength equal to $\lambda' = 632.8$ nm, and the normalized intensity correlation function $g^{(2)}(\tau) = \langle I(0)I(\tau) \rangle / \langle I^2 \rangle$ of the scattering intensity $I(\tau)$ was obtained through a multi-angle detection system by Brookhaven Co. with a TurboCo correlator. To ensure the proper ensemble average, a large pinhole ($400 \mu\text{m}$ of diameter) was placed before the photon detector so the final average was a result of different positions across the samples. The MSD of the probe particles was estimated experimentally as³⁶

$$\langle \Delta r^2(\tau) \rangle = -\frac{6}{q^2} \ln \left(\frac{g^{(2)}(\tau) - 1 - \sigma + \beta}{\beta} \right)^{1/2}, \quad (40)$$

where $q = (4\mu\pi/\lambda')\sin(\theta/2)$ is the modulus of the scattering vector, which is obtained from the wavelength λ' , the refraction index of water $\mu = 1.331$, and the scattering angle θ . The parameters β and σ in Eq. 40 correspond to the extrapolation of the autocorrelation function for $\tau \rightarrow 0$ for homodyne scattering (in this case, standard polystyrene particles in aqueous solution) and heterodyne scattering (polystyrene particles in the gels), respectively⁴¹.

5.3. Gelation process in laponite gels

First, to illustrate the application of the KVMH model in the description of a very heterogeneous gel, we include here measurements related to the gelation process of laponite gels. In particular, we considered 10 mL of laponite hydrogel synthesized in 3% m/m concentration, together with $5 \mu\text{L}$ of solution with polystyrene particles with radius $a = 0.5 \mu\text{m}$ (Spherotech). The sample was stirred and sonicated for some minutes to mix the laponite in the solution. The measurements were made at $T = 298$ K along 136 hours, with accumulation times of one hour to obtain $g^{(2)}(\tau)$ and for a scattering angle equal to 90° .

Figure 5(a) exhibits the time-dependent diffusion coefficient $D(\tau)$ for different gelation times τ_w . The results show the decrease of the diffusion coefficient as τ_w increases, indicating further entrapment of the particles in the microstructures of the gel. Clearly, the ageing of the gel is marked by a slightly decrease in the material's heterogeneity, as it can be inferred from the increase in the value of p observed in Fig. 5(b). Interestingly, previous research has established that this gel is composed of micron-sized aggregates exhibiting fractal behaviour^{42,43}. Indeed, in this case, one can relate the exponent p to the spectral dimension d_s that characterizes the network topology⁴⁴, since the time-dependent diffusion coefficient is expected to behave as³⁶ $D(\tau) \propto \tau^{-d_s/2}$ at long times. In this regime, Eq. 19 gives $D(\tau) \propto \tau^{-(1+p)}$, so p and d_s are expected to be related as $d_s = 2(1+p)$. In particular, the saturation value of 0.2 observed for p in Fig. 5(b) corresponds to $d_s = 2.4$, which is a value that is close to that observed for different kinds of gels³⁶.

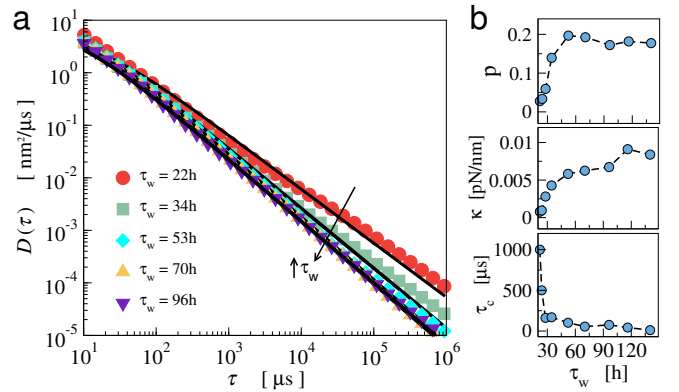


FIG. 5. (a) Time-dependent diffusion coefficient $D(\tau)$ of polystyrene particles ($a = 0.5 \mu\text{m}$) during the gelation of a Laponite gel in room temperature ($T = 298$ K) at different gelation times τ_w . (b) Parameters p , κ , and τ_c obtained through the fit of $D(\tau)$ obtained for the KVMH model (continuous black lines, Eq. 19) to the experimental data shown in (a) as a function of τ_w .

Here it is worth noting that the fit of the expressions obtained from the KVMH model to the experimental data also provides estimates for κ and τ_c . The increase in the material stiffness can be inferred from the increase in κ in Fig. 5(b), and the observed decay in τ_c reflects the further entrapment of the probe particles.

5.4. Heterogeneity-related effects in polyacrylamide gels

Finally, to show a case where the semisolid material is not so heterogeneous, we present additional results that were obtained for a polyacrylamide gel. The gel was synthesized using acrylamide (A8887), bis-acrylamide (M7279), tetramethylethylenediamine (TEMED, T7024) and ammonium persulfate (APS, A3678), all purchased from SIGMA-ALDRICH. The synthesis was made at room temperature ($T \cong 298$ K) using the ratio of acrylamide and bis-acrylamide equal to 30 : 1, with total concentration equal 4.14% m/m. After this was added $5 \mu\text{L}$ of solution with polystyrene particles with radius $a = 0.5 \mu\text{m}$. To start the reaction, 5 mL of APS solution with 0.404% m/m and $10 \mu\text{L}$ of TEMED was added. The sample was left to react at 0°C overnight. The measurements were made in room temperature, i.e., $T = 298$ K, with 3 hours of duration, 6 accumulations (average over 6 measurements) at different sample positions and for a scattering angle equal to 40° . The pinhole was set, as before, to $400 \mu\text{m}$.

Figure 6 shows that although the KVMH model is still more adequate to describe the experimental results, the discrepancy between the fits of the two models to the experimental data is rather small. This occurred because of the high value of $p = 5.98$. As $p \gg 1$, the distribution of local spring constants $\rho(\varepsilon)$, Eq. 21, becomes narrower with the more prominent peak around the mean $\bar{\varepsilon} = \kappa$.

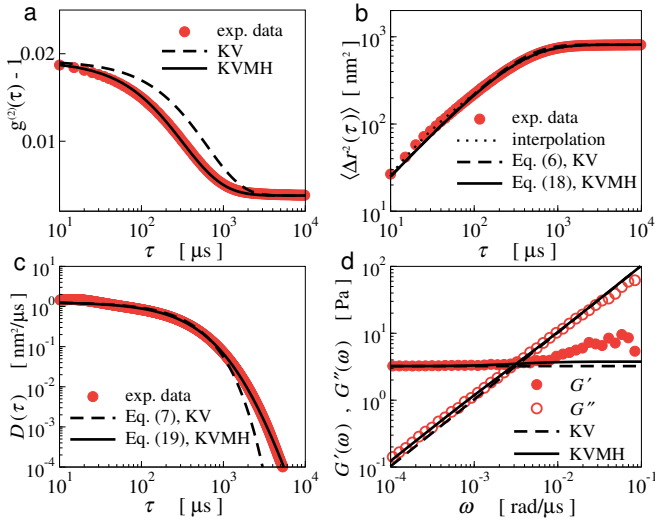


FIG. 6. Comparison between the experimental data obtained for a polyacrylamide gel (filled red circles) and the theoretical expressions from the usual KV model with $T = 298$ K, $\kappa = 1.52 \times 10^{-2}$ pN/nm, $\tau_c = 636.47 \mu\text{s}$, and the KVMH model with the same parameters and $p = 5.98$. (a) Intensity-normalized correlation function $g^{(2)}(\tau) - 1$. (b) MSD $\langle \Delta r^2(\tau) \rangle$ after 24h. (c) Time-dependent diffusion coefficient $D(\tau)$ (here the experimental estimates were obtained from a smoothed interpolation⁴⁰ using Eq. 38 with $\varphi = 0.4$). (d) Storage modulus $G'(\omega)$ (filled circles) and loss modulus $G''(\omega)$ (open circles), obtained from $\langle \Delta r^2(\tau) \rangle$ via Eqs. 2 and 3, with $\hat{J}(\omega)$ obtained through Eq. 39 using the numerical method described in Ref.²⁵.

This is precisely the case of the semisolid Kelvin-Voigt described in Sec. 2, where the material is characterized by just one spring constant κ . Thus, this result indicates that the polyacrylamide gel produced in our laboratory is reasonably homogeneous.

6. CONCLUDING REMARKS

In this work, we established a theoretical approach that generalizes the Kelvin-Voigt model to take into account the micro-heterogeneities observed in semisolid viscoelastic materials. Our model naturally introduces the micro-heterogeneities in the context of microrheology, with the average over the various mesoscopic regions theoretically performed here being equivalent to the experimental measurements using the multiple particle tracking technique²¹.

By considering both experiments and simulations we were able to validate our theoretical results, including the expressions for the MSD (Eq. 18), for the time-dependent diffusion coefficient (Eq. 19), and for the position distributions (Eq. 28 for short times and Eq. 29 for later times). Interestingly, our numerical and analytical findings indicate a direct relationship between the micro-heterogeneities of local spring constants, the non-

Gaussianity of the van Hove distributions $f(x, \tau)$, and the power-law behaviour of $D(\tau)$ at long times. Hence, the obtained expressions for $\langle \Delta x^2(\tau) \rangle$ and $D(\tau)$ can be used by experimental rheologists to yield estimates for the exponent p , so they provide a way to infer the relevance of the micro-heterogeneities to the response of KV-like semisolid materials.

Finally, it is worth noting that although we were not able to derive exact analytical expressions for the shear moduli $G'(\omega)$ and $G''(\omega)$ for the KVMH model, we showed that both moduli can be obtained numerically from the fit of our expressions to the experimental data through the method described in Ref.²⁵. This model-fitting procedure allows one to extract reliable estimates for the shear moduli even when the MSD displays noisy behaviour at long times, as it usually occurs to experimental data obtained from microrheology techniques.

Acknowledgements: T. N. Azevedo thanks the scholarship from CAPES, and L. G. Rizzi acknowledges the support from the Brazilian agency CNPq (Grant N^o 312999/2021-6). The authors also thank the computational resources made available by GISC-UFV.

Conflicts of interest: There are no conflicts to declare.

Data availability: The data that support the findings of this study are available from the corresponding author upon reasonable request.

Author Contributions: **T. N. Azevedo.** Investigation. Data curation. Formal analysis. Software. Writing - original draft. Writing - review & editing. **K. M. Oliveira.** Investigation. Data curation. Formal analysis. Writing - original draft. **H. P. Maia.** Investigation. Data curation. Formal analysis. **A. V. N. C. Teixeira.** Investigation. Data curation. Formal analysis. Methodology. Supervision. Validation. Writing - review & editing. **L. G. Rizzi.** Conceptualization. Investigation. Data curation. Formal analysis. Funding acquisition. Methodology. Software. Visualization. Project administration. Supervision. Validation. Writing - original draft. Writing - review & editing.

REFERENCES

- ¹W. W. Graessley, *Polymeric liquids and Networks: Structure and Properties* (Taylor & Francis, 2003).
- ²M. T. Valentine, P. D. Kaplan, D. Thota, J. C. Crocker, T. Gisler, R. K. Prud'homme, M. Beck, and D. A. Weitz, "Investigating the microenvironments of inhomogeneous soft materials with multiple particle tracking," *Phys. Rev. E* **64**, 061506 (2001).
- ³J. Apgar, Y. Tseng, E. Fedorov, M. B. Herwig, S. C. Almo, and D. Wirtz, "Multiple-particle tracking measurements of heterogeneities in solutions of actin filaments and actin bundles," *Biophys. J.* **79**, 1095–1106 (2000).
- ⁴M. Shayegan and N. R. Forde, "Microrheological characterization of collagen systems: From molecular solutions to fibrillar gels," *PLOS ONE* **8**, 1–12 (2013).

- ⁵H. A. Houghton, I. A. Hasnain, and A. M. Donald, “Particle tracking to reveal gelation of hectorite dispersions,” *Eur. Phys. J. E* **25**, 119 (2008).
- ⁶A. M. Corrigan and A. M. Donald, “Particle tracking microrheology of gel-forming amyloid fibril networks,” *Eur. Phys. J. E* **28**, 457 (2009).
- ⁷A. Aufderhorst-Roberts, W. J. Frith, and A. M. Donald, “Microscale kinetics and heterogeneity of a pH triggered hydrogel,” *Soft Matter* **8**, 5940 (2012).
- ⁸A. Aufderhorst-Roberts, W. J. Frith, and A. M. Donald, “A microrheological study of hydrogel kinetics and microheterogeneity,” *Eur. Phys. J. E* **37**, 44 (2014).
- ⁹A. H. Krall and D. A. Weitz, “Internal dynamics and elasticity of fractal colloidal gels,” *Phys. Rev. Lett.* **80**, 778 (1998).
- ¹⁰T. Savin and P. S. Doyle, “Statistical and sampling issues when using multiple particle tracking,” *Phys. Rev. E* **76**, 021501 (2007).
- ¹¹L. G. Rizzi, “Microrheological approach for the viscoelastic response of gels,” *J. Rheol.* **64**, 969 (2020).
- ¹²Y. Tseng, K. M. An, and D. Wirtz, “Microheterogeneity controls the rate of gelation of actin filament networks,” *J. Biol. Chem.* **277**, 18143–18150 (2002).
- ¹³Y. Tseng and D. Wirtz, “Dendritic branching and homogenization of actin networks mediated by arp2/3 complex,” *Phys. Rev. Lett.* **93**, 258104 (2004).
- ¹⁴J. Quintanilla, “Microstructure and properties of random heterogeneous materials: A review of theoretical results,” *Polym. Eng. Sci.* **39**, 559–585 (1999).
- ¹⁵J. D. Ferry, *Viscoelastic Properties of Polymers*, 3rd ed. (John Wiley & Sons, New York, 1980).
- ¹⁶M. A. Rao, *Rheology of Fluid, Semisolid, and Solid Foods: Principles and Applications*, 3rd ed. (Springer, New York, 2014).
- ¹⁷P. Domínguez-García, G. Dietler, L. Forró, and S. Jeney, “Filamentous and step-like behavior of gelling coarse fibrin networks revealed by high-frequency microrheology,” *Soft Matter* **16**, 4234–4242 (2020).
- ¹⁸S. Shabaniverki and J. J. Juárez, “Characterizing gelatin hydrogel viscoelasticity with diffusing colloidal probe microscopy,” *J. Colloid Interface Sci.* **497**, 73–82 (2017).
- ¹⁹W. Nantasetphong, Z. Jia, A. Amirkhizi, and S. Nemat-Nasser, “Dynamic properties of polyurea-milled glass composites part i: Experimental characterization,” *Mech. Mater.* **98**, 142–153 (2016).
- ²⁰J. P. Rich, G. H. McKinley, and P. S. Doyle, “Size dependence of microprobe dynamics during gelation of a discotic colloidal clay,” *J. Rheol.* **55**, 273–299 (2011).
- ²¹L. G. Rizzi and M. Tassieri, “Microrheology of biological specimens,” in *Encyclopedia of Analytical Chemistry* (John Wiley & Sons, 2018) pp. 1–24.
- ²²T. A. Waigh, “Advances in the microrheology of complex fluids,” *Rep. Prog. Phys.* **79**, 074601 (2016).
- ²³T. M. Squires and T. G. Mason, “Fluid mechanics of microrheology,” *Annu. Rev. Fluid Mech.* **42**, 413–438 (2010).
- ²⁴T. G. Mason, “Estimating the viscoelastic moduli of complex fluids using the generalized Stokes-Einstein equation,” *Rheol. Acta* **39**, 371–378 (2000).
- ²⁵R. M. L. Evans, M. Tassieri, D. Auhl, and T. A. Waigh, “Direct conversion of rheological compliance measurements into storage and loss moduli,” *Phys. Rev. E* **80**, 012501 (2009).
- ²⁶T. N. Azevedo and L. G. Rizzi, “Microrheology of filament networks from brownian dynamics simulations,” *J. Phys.: Conf. Ser.* **1483**, 012001 (2020).
- ²⁷D. T. Gillespie, “Fluctuation and dissipation in Brownian motion,” *Am. J. Phys.* **61**, 1077 (1993).
- ²⁸G. E. Crooks, *Field Guide to Continuous Probability Distributions* (2019).
- ²⁹I. S. Gradshteyn and I. M. Ryzhik, *Table of Integrals, Series, and Products* (Academic Press, San Diego, 2007).
- ³⁰A. Krall, Z. Huang, and D. Weitz, “Dynamics of density fluctuations in colloidal gels,” *Physica A* **235**, 19–33 (1997).
- ³¹A. D. Dinsmore, V. Prasad, I. Y. Wong, and D. A. Weitz, “Microscopic structure and elasticity of weakly aggregated colloidal gels,” *Phys. Rev. Lett.* **96**, 185502 (2006).
- ³²A. Zaccone, H. H. Winter, M. Siebenbürger, and M. Ballauff, “Linking self-assembly, rheology, and gel transition in attractive colloids,” *J. Rheol.* **58**, 1219–1244 (2014).
- ³³M. Mours and H. H. Winter, “Mechanical spectroscopy of polymers,” in *Experimental methods in polymer science*, edited by T. Tanaka (Academic Press, 2000) Chap. 5, p. 495.
- ³⁴D. Hexner, A. J. Liu, and S. R. Nagel, “Linking microscopic and macroscopic response in disordered solids,” *Phys. Rev. E* **97**, 063001 (2018).
- ³⁵D. Hexner, A. J. Liu, and S. R. Nagel, “Role of local response in manipulating the elastic properties of disordered solids by bond removal,” *Soft Matter* **14**, 312 (2018).
- ³⁶A. V. Teixeira, E. Geissler, and P. Licinio, “Dynamic scaling of copolymer gels comprising nanoparticles,” *J. Phys. Chem. B* **111**, 340 (2007).
- ³⁷P. Virtanen, R. Gommers, T. E. Oliphant, M. Haberland, T. Reddy, D. Cournapeau, E. Burovski, P. Peterson, W. Weckesser, J. Bright, S. J. van der Walt, M. Brett, J. Wilson, K. Jarrod Millman, N. Mayorov, A. R. J. Nelson, E. Jones, R. Kern, E. Larson, C. Carey, Í. Polat, Y. Feng, E. W. Moore, J. VanderPlas, D. Laxalde, J. Perktold, R. Cimrman, I. Henriksen, E. A. Quintero, C. R. Harris, A. M. Archibald, A. H. Ribeiro, F. Pedregosa, P. van Mulbregt, and S. . Contributors, “SciPy 1.0: Fundamental Algorithms for Scientific Computing in Python,” *Nature Methods* **11**, 261 (2005).
- ³⁸F. K. Oppong, P. Coussot, and J. R. de Bruyn, “Gelation on the microscopic scale,” *Phys. Rev. E* **78**, 021405 (2008).
- ³⁹B. R. Dasgupta and D. A. Weitz, “Microrheology of cross-linked polyacrylamide networks,” *Phys. Rev. E* **71**, 021504 (2005).
- ⁴⁰H. L. Weinert, “A fast compact algorithm for cubic spline smoothing,” *Computational Statistics & Data Analysis* **53**, 932–940 (2009).
- ⁴¹B. Berne and R. Pecora, *Dynamic Light Scattering: With Applications to Chemistry, Biology, and Physics* (Dover Publications Inc., New York, 2000).
- ⁴²F. Pignon, J.-M. Piau, and A. Magnin, “Structure and pertinent length scale of a discotic clay gel,” *Phys. Rev. Lett.* **76**, 4857–4860 (1996).
- ⁴³F. Pignon, A. Magnin, J.-M. Piau, B. Cabane, P. Lindner, and O. Diat, “Yield stress thixotropic clay suspension: Investigations of structure by light, neutron, and x-ray scattering,” *Phys. Rev. E* **56**, 3281–3289 (1997).
- ⁴⁴S. Havlin and D. Ben-Avraham, “Diffusion in disordered media,” *Adv. Phys.* **51**, 187–292 (2002).